Kent Academic Repository

Full text document (pdf)

Link to record in KAR

https://kar.kent.ac.uk/95464/

Document Version

UNSPECIFIED

Catastrophic disruption by hypervelocity impact of multi-layered spherical ice targets

M.J. Burchell [*], K.H. Harriss

Centre for Astrophysics and Planetary Science, School of Physical Sciences, University of Kent, Canterbury, Kent, CT2 7NH, United Kingdom

ARTICLE INFO

ABSTRACT

The catastrophic disruption of tri-layered spherical icy bodies is reported. The bodies are 19 cm in total diameter, with a central core, an intermediate water layer and an icy surface (each layer respectively approximately 25, 55 and 20% of the total radius). Their response to high-speed impact is investigated at laboratory scales by firing 1.5 mm diameter glass spheres at the targets at speeds in the range $0.9 - 3.2$ km s^{-1} and an ice layer thickness normalised to projectile diameter of typically $20 - 30$. The energy density to just break apart such a body (defined as an event where the mass of the largest fragment post-impact is ½ the original target mass) is (3.1 ± 0.1) J kg^{-1}. This is significantly less than that found for similar sized solid ice spheres (18 ± 0.7) J kg^{-1}, water filled ice spheres (16.25 ± 1.35) J kg^{-1} or hollow ice spheres (25.5 ± 0.5) J kg^{-1} indicating that the presence of a solid layer beneath an internal ocean, can influence disruption, effectively weakening the body.

1. Introduction

The problem considered here is the catastrophic disruption of tri-layered spherical bodies with an icy surface, intermediate liquid layer and a solid core. This is inspired by the presence in the Solar System of the icy satellites of the outer planets. In several cases, the icy exteriors of these bodies are known to cover global oceans with a solid core in the centre of the body e.g. Europa (e.g. [1–3]), Ganymede (e.g. [4]), Callisto (e.g. [5]), Enceladus (e.g. [6–8]) and Titan (e.g. [9–11]). A major evolutionary driver of any solar system body is impact by another body. Whilst impact by small bodies at low energy will leave a crater in the surface ice, as the impact energy density (defined as Q, crudely the kinetic energy of the impactor divided by the mass of the target) increases the surface ice layer is penetrated, then at higher Q the target body becomes disrupted, and, if there is sufficient energy, the fragments disperse against their own self-gravity. At the highest Q values the result is a catastrophically disrupted body. A critical value of Q, called Q*, is taken to mark the transition to a catastrophically disrupted state, and is defined as that where the largest surviving fragment after impact has a mass equal to half that of the original intact body.

In this present work, the response of icy tri-layered spherical bodies to impacts is considered experimentally using decimetre scale model targets. In previous work in the laboratory, we have considered how impact cratering proceeds in bi-layered semi-infinite ice targets [12], and determined the Q* value (i.e. observed catastrophic disruption) in: solid ice spherical targets ([13], and see previous work, e.g. [14]); ice shell targets with hollow interiors [15]; and ice shell targets with liquid (water) interiors [16]. Here we extend the sequence by looking at the results of impacts on ice shell targets with a solid core and an intermediate liquid water layer (see Fig. 1).

2. Method

The ice targets were 19.3 cm in diameter. They were made in a similar fashion to the water filled ice spheres described in [16]. This involves filling a balloon with cooled, purified water and freezing it in a mould. However, before inserting the water under pressure into the balloon, a solid sphere of acrylic, 5.0 ± 0.1 cm in diameter (density 1180 kg m^{-3}, mass 0.077 kg), was also inserted into the balloon. The choice of acrylic was made as a convenient starting point for such work and a suitable sized core was to hand. The core was suspended from a string which ran through the neck of the balloon. The string length was selected so that the core hung in the centre of the inflated balloon. Red dye was sometimes used in the water to show any penetration of the water into the ice shell after impact, via any fractures that may have opened (again similar to [16]). To ensure the core is visible (given that it was transparent acrylic inside water beneath a shell of transparent ice), it was necessary to mark it in some fashion. Accordingly, the core was

---

* Corresponding author.
E-mail address: m.j.burchell@kent.ac.uk (M.J. Burchell).

either wrapped in yellow and black tape or, in later shots, the core was painted yellow (this had no apparent influence on the results themselves). During freezing, the mould was placed in a freezer, set to -25°C. The duration of storage in the freezer determined the depth of the ice shell. A freezing time of 24hrs for example, produced a shell 4 cm thick, but left the interior still liquid.

The shots were carried out in the Univ. of Kent two-stage light gas gun [17, 18]. The targets were placed in the gun, whose target chamber was evacuated to 50 mbar pre-shot. This used a quick pump-down time of about 20 minutes. Experience over many years, has shown that during this time, the ice target temperature only increases by a few °C or less, and the ice is still frozen solid at impact. The projectiles were 1.5 mm diameter, glass projectiles, whose speed was measured in-flight by their passage through two laser beams focussed onto photo-diodes read out on a high speed digital oscilloscope. Interruption of the beams changes the photodiode outputs, providing timing signals, which combined with the known separation of the two lasers (0.499 m), permits speed measurements to within ±1%. In some shots, high speed videos were obtained using a Panasonic HXWA30 camera which took images at 60 fps; whilst too slow to show crack propagation, the framing rate was sufficient to track ejecta.

The targets (and fragments) were removed from the gun within a few minutes of the shot. This quick removal time meant there was no measureable post-shot melting of the target or large fragments before their analysis. When the ice shell had been cratered rather than penetrated or disrupted, the water layer was retained in the target and the crater depth and diameter in the ice surface layer were measured. When penetration occurred, the water content was partially reduced by flow through the hole under gravity, but if the target still maintained its integrity post-shock, the hole size was measured (e.g. see Fig. 2 for an example target after a penetrating impact). When the target broke up during the impact, the water was lost totally into the target chamber, but the mass of the four largest surviving surface layer ice fragments was measured.

3. Results

There were a total of 10 shots in this program, each of which had an acrylic core in the centre of an ice shell with an intermediate water layer (see Table 1). Shots 1 – 8 (all at normal incidence) were used to determine Q^*. Data for two additional shots are also reported (shots 9 and 10). Shot 9, impact speed 1.97 km s^{-1} (at normal incidence), has incomplete data (part of the ice shell around the crater sheared off in the impact, see comments in Table 2 for details) and is thus not included in the main analysis to determine Q^*; it is however discussed later. In shot 10 (impact speed 3.24 km s^{-1}), the projectile struck away from the target equator, and was thus a non-normal incidence impact, at about 30° from the vertical. Such non-normal incidence impacts couple the incident energy (and momentum) less well into the target (see Discussion), and so shot 10 is not included in the determination of Q^*, but is included here to show the effects of non-normal incidence.

The 8 events (shots 1 – 8) used to determine Q^* have their data for the ratio of the mass of the largest target fragment post-shot (m_f) to the initial target mass (m_i), vs. the impact energy density Q shown in Fig. 3. At relatively low Q (< 1 J kg^{-1}), there is minor cratering in the ice shell. As Q increases, the volume of the crater initially increases, and radial fractures (typically 2 – 3) appear in the ice surrounding the target (see Comments in Table 2, where we also give the ratio of ice shell thickness/ projectile diameter t/d). In the range $2 < Q < 2.5$ J kg^{-1}, increased fracturing of the target occurred. This included an increased number of radial fractures (up to about 5, which reached further away from the crater. Concentric fractures also appeared around the impact site. However, the ice layer was not penetrated. At around 2.5 J kg^{-1}, the ice shell was just penetrated in the thinner shell examples ($t/d \approx 12$ - 14) but not the thicker cases ($t/d \approx 23$ - 29).

Shot 9 (at 1.97) km s^{-1} has incomplete data due to an un-expected feature – namely the front of the ice shell around the impact point sheared off under impact (see Fig. 4). This sheared-off region contained an intact crater, which just, marginally, penetrated the ice-shell. The diameter of this sheared-off disk was 14.8 cm, with a height of 4.2 cm. This behaviour of the front face (as seen from the impact) shearing-off has been observed before for impacts on solid ice spheres (see [13])

(a) Ice (top) over various substrates (water, sand, rock..)

(b) Solid ice   (c) Hollow ice   (d) Water filled ice shell   (e) Water filled ice shell, plus solid core

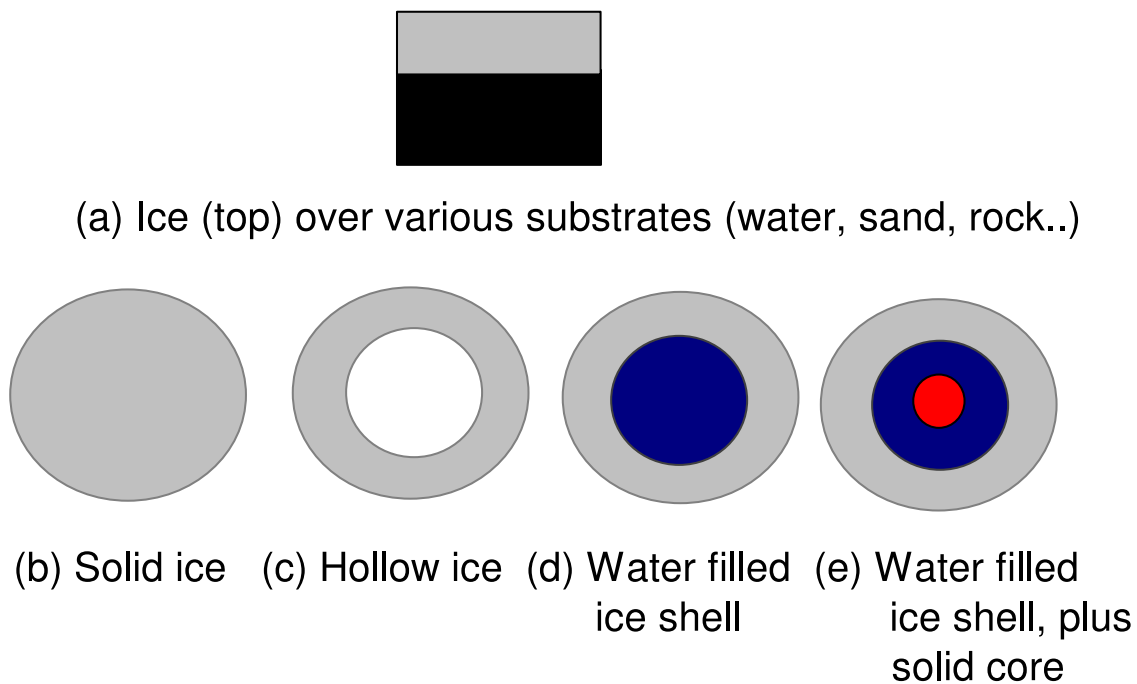**Fig. 1.** Internal structures of targets with an icy surface. (a) An ice layer over a substrate of different materials such as water, sand and basalt [12]. (b – e) Spherical rather than semi-infinite target are considered next. (b) is solid ice (e.g. [13], (c) is a hollow ice shell [15], (d) is a water filled ice sphere [16], and (e) is a water filled ice sphere with a central solid core (this work).

Fig. 2. Ice target after impact at 2.09 km s^{-1} (shot 6), showing a penetrating crater (note the original interior water has been drained away). The core can be seen wrapped in yellow tape (no longer supported by water the core has swung to one side). The sphere diameter is 19.3 cm. The penetrating hole in surface ice layer was approx. 4.9 by 7.6 cm, with an equivalent diameter if circular of 6.8 cm.

Table 1

Shot details. Shots 1 – 8 were used to determine Q*. Details of two additional shots (9 and 10) are also given and are used in other parts of the analysis and discussion.

Shot number	Impact Speed (km s^{-1})	Energy (J)	Initial Target mass (kg)	Impact Energy density Q (J kg^{-1})	Final Target Mass (kg)	Final / initial target mass
1	0.92	1.85	3.575	0.52	3.488	0.976
2	0.94	1.96	3.513	0.56	3.433	0.967
3	1.96	8.50	3.513	2.42	3.151	0.897
4	1.96	8.50	3.635	2.33	2.795	0.769
5	1.97	8.59	3.499	2.45	2.668	0.763
6	2.09	9.66	3.596	2.69	2.100	0.584
7	2.42	13.0	3.427	3.79	1.054	0.308
8	2.93	19.0	3.511	5.41	0.795	0.226
Additional	shots					
9	1.97	8.59	3.558	2.41	Not. Meas.	Not meas.
10	3.24	23.2	3.617	6.41	2.712	0.750

and is not assumed related to the core being off centre (it was stuck to the inner ice shell at the rear of the target as seen from the impact point). On a large, self-gravitating body, such a fragment will sit in place, it is only here, with a horizontal impact at laboratory scale that it falls from the parent body. Thus it is an ice-shell penetrating impact, but not a catastrophic disruption event. The normal details of a crater forming event can be seen in this event, a fast moving ejecta plume (Fig. 4b), followed by a growing crown of larger ejecta (Fig. 4c), and then slower moving pieces of even larger spall fragments. The impact occurred between two frames of the video, placing an upper limit on the accuracy of its time of impact of 0.017s. Thus the t = 0 moment shown in Fig. 4b, may be as much as 0.017 s after the actual impact. In the time of $\leq$ 0.017s, the plume has already reached a height of 2.6 cm, so is travelling at $\geq$ 1.6 m s^{-1}. At this stage, no large-scale fractures are visible in the ice. Such fractures have already appeared at t = +0.017 s (Fig. 4c) by which time the front of the high speed plume has passed out of the field of view, indicating a speed $\geq$ 3.8 m s^{-1}. Given that the radius of the region which subsequently detaches is 7.4 cm, and the fractures have propagated between the frames shown in Fig. 4b,c, the speed of fracture formation is

$\geq$ 4.3 m s^{-1}. Note that these speeds are likely a gross underestimate due to the low framing rate and the limited field of view. Indeed it has previously been shown for ice that shock wave propagation occurs at speeds of order km s^{-1}, much greater than can be measured here (e.g. [19, 20]). Burchell *et al.* [16] observed the growth of the cracks in similar ice spheres and measured the propagation speed (using an ultra-high speed camera) to be of order 667 m s^{-1}, as expected this is considerably faster than the lower bounds found here. As time moves forward in the impact in Fig 4, more ejecta appears, forming the classic crown around the impact site (Fig. 4d, t = +0.051 s). By t = +0.10 s, larger, slower moving spall fragments have lifted off the surface (examples of large spall fragments are labelled A and B). Tracking these larger spall fragments from frame to frame, gives a speed of ~ 0.2 m s^{-1} for fragment A and ~ 0.19 m s^{-1} for B.

The growth of cracks in ice shells over liquid interiors which undergo hypervelocity impacts has been reported previously [16], where the sequence of events was broadly that as here. The first impact plume appeared before cracks propagated in the ice. Both radial and concentric crack features then appeared, with lower speed impacts producing mostly radial cracks and concentric features only appeared as impact speed increased.

In the experiments reported herein, catastrophic failure of the target occurred at just above 3 J kg^{-1}. To better identify the Q* value, a power law fit was made in Fig. 3 to the data in the Q range where the mass loss increased rapidly with Q, (shots 3 – 8, i.e. above 2 J kg^{-1}). The result was:

$$m_{final}/m_{initial} = (4.06 \pm 1.42)Q^{-(1.86 \pm 0.37)}, r^2 = 0.9342, \qquad (1)$$

where r is the regression coefficient. Given that Q* is defined as being when the final/initial mass ratio = 0.5, this implies Q* = 3.08 J kg^{-1}. The associated uncertainty is of order $\pm$ 0.1 J kg^{-1}, giving a Q* value of (3.1$\pm$0.1) J kg^{-1}. This is significantly lower than the Q* value for similar sized water filled ice spheres with no cores and for solid ice spheres, where Q* = (16.25 $\pm$ 1.35) and (18 $\pm$ 0.7) J kg^{-1} respectively (see Table 3).

The role of the surface ice layer thickness in influencing Q* is not fully investigated here and the shots only include relatively thick ice shells. The ice thickness can be taken relative to projectile size, i.e. the thickness of the ice shell (*t*) divided by projectile diameter (*d*) which is *t*/

Table 2
Ice shell parameters and details of impact crater size.

| Shot number	Impact Speed(km s^{-1})	Ice shell thickness t (mm)	Ice shell thickness/ proj. dia. (t/d)	Crater dia. (mm)	Crater depth (mm)	Comment
1	0.91	19	13	35	9.1	Impact crater formed in shell
2	0.94	35	23	34	5.1	Impact crater formed in shell
3	1.96	34	23	56	14.5	Impact crater formed without penetrating the shell. Cracks were observed in the ice shell and dye entered cracks from the interior water layer, but didn't reach the ice surface
4	1.96	39	26	88	8.9	Crater formed, no penetration
5	1.97	43	29	85	5.8	Dye entered cracks in interior but didn't reach surface
6	2.09	18	12	68	N/A	Impact crater formed and penetrated into interior
7	2.42	33	22	75	Not meas.	Crater formed, target then broke when moved. Masses of the four largest ice fragments post shot were: 1054, 388, 283 and 200 g.
8	2.93	33	22	-	N/A	Complete disruption. Masses of the four largest ice fragments post shot were: 795, 366, 282 and 155 g.
9	1.97	21	14	47	N/A	An entire disc, 148 mm in dia. and centred on the impact point, separated from the rest of the ice. This then fell off the target under the influence (under gravity), releasing the interior water. The crater in this detached disk just penetrated the ice shell.
10	3.24	41	27	75	6.67	Glancing impact
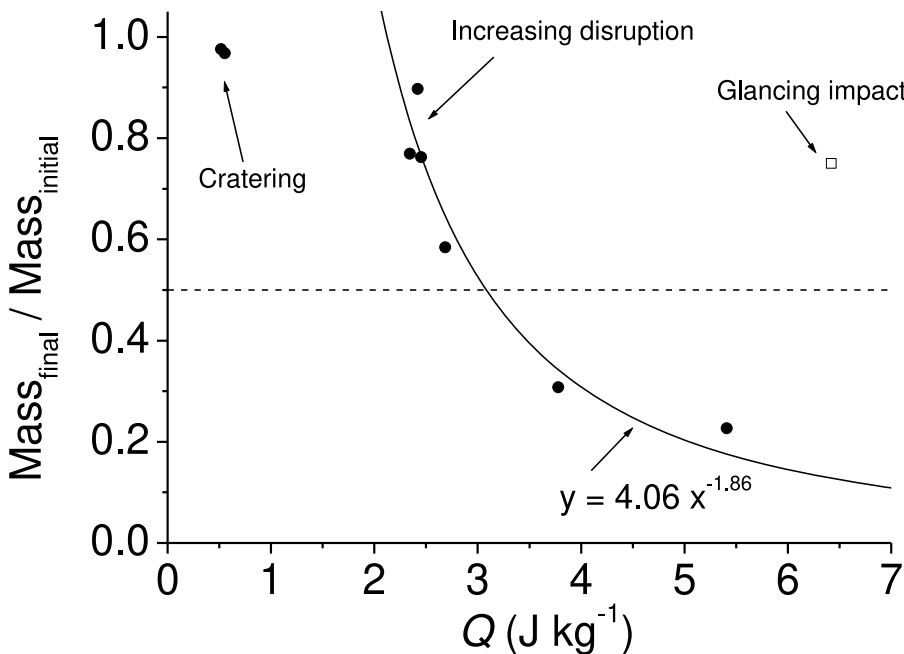
Fig. 3. The ratio of mass of largest fragment (post-impact) to initial target mass m_f / m_i, vs. impact energy density Q for shots 1 – 8 (•) at normal incidence, and shot 10 (□) non-normal incidence. The horizontal dashed line shows $m_f / m_i = 0.5$, which indicates catastrophic disruption. The value of Q in the data at $m_f / m_i = 0.5$ is taken as the critical value of energy density Q^*. Shots 1 and 2 are in the purely cratering regime and remove relatively little mass. Shots 3 – 8 (normal incidence, $Q > 2$ J kg^{-1}) remove ever increasing amounts of target mass and enter the catastrophic disruption regime. The fit shown (solid line) is to the normal incidence data for $Q > 2$ J kg^{-1}, (shots 3 – 8) where the mass ratio changes rapidly, and suggests $Q^* = 3.1 \pm 0.1$ J kg^{-1}. The data point from shot 10 (top right) is from a non-normal incidence (30° from the vertical) impact at 3.24 km s^{-1}. Shot 10 has a Q value of 6.42 J kg^{-1}, well above the Q^* value, however it did not disrupt the target, indicating how oblique impacts couple their energy less effectively into a target.

d (see Table 2 for relevant values). Here, 6 of the 8 good impacts have t/d in the range 20 – 30, representing relatively thick ice (shots 2 – 5 and 7 - 8). Of the other two impacts (shots 1 and 6), both had t/d in the range 10 – 20, still thick but not quite as thick as in the other shots. However, one of these two low t/d events (shot 1), was an impact at low Q, and resulted in cratering rather than penetration of the ice, and was thus not used in the fit, eqn. 1, which determined Q^*. That only leaves one event used to determine Q^* which had a low t_i/d_p value (= 12), outside the range of the other shots (= t_i/d_p 20 – 30). The datum from this impact (shot 6, impact speed 2.09 km s^{-1}) follows the trend from the other shots, indeed if this datum were excluded from the fit in Fig. 3, the value of Q^* changes by just 0.05 J kg^{-1}, which is half the quoted uncertainty in the result. We thus conclude that the work is not too sensitive to t/d when this is large, and the result for Q^* found here is appropriate for relatively thick ice shells.

The datum from the impact at a glancing angle of incidence (shot 10) is shown with an open square on Fig 3. This impact was at 3.24 km s^{-1}, with a Q value of 6.42 J kg^{-1}. Whilst this is above the Q^* value for normal incidence impacts, it has not disrupted the target. In general,

oblique impacts couple the incidence energy/momentum less efficiently into the interior of a body, resulting in longer, shallower craters (e.g. see [21] for laboratory experiments of oblique impacts on ices). How this effects catastrophic disruption is discussed for example in [22. 23], who show that it results in a larger effective Q^* as less of the impactor mass interacts with the target. This evolution of Q^* vs. impact angle for glass and gypsum is shown experimentally in [24], with an increase in Q^* as impact angle deviates from normal incidence. Separately, it is suggested in [25] that, based on hydrocode simulations for large bodies, several multiples of the value of Q^* at normal incidence, are required to obtain the effective Q^* in an oblique impact at 30 - 45° from the vertical, compatible with what is seen here.

In the two catastrophic disruption events (shots 7 and 8, impact speeds 2.42 and 2.93 km s^{-1} and Q values 3.78 and 5.41 J kg^{-1} respectively) the masses of the 4 largest fragments post-shot are given in the final (Comment) column in Table 2, and the cumulative fragment mass distribution for the largest fragments is shown in Fig. 5a. Both distributions in Fig. 5a appear as near straight lines on a log-log plot, with slopes indicating that fragment mass is still sharply decreasing from
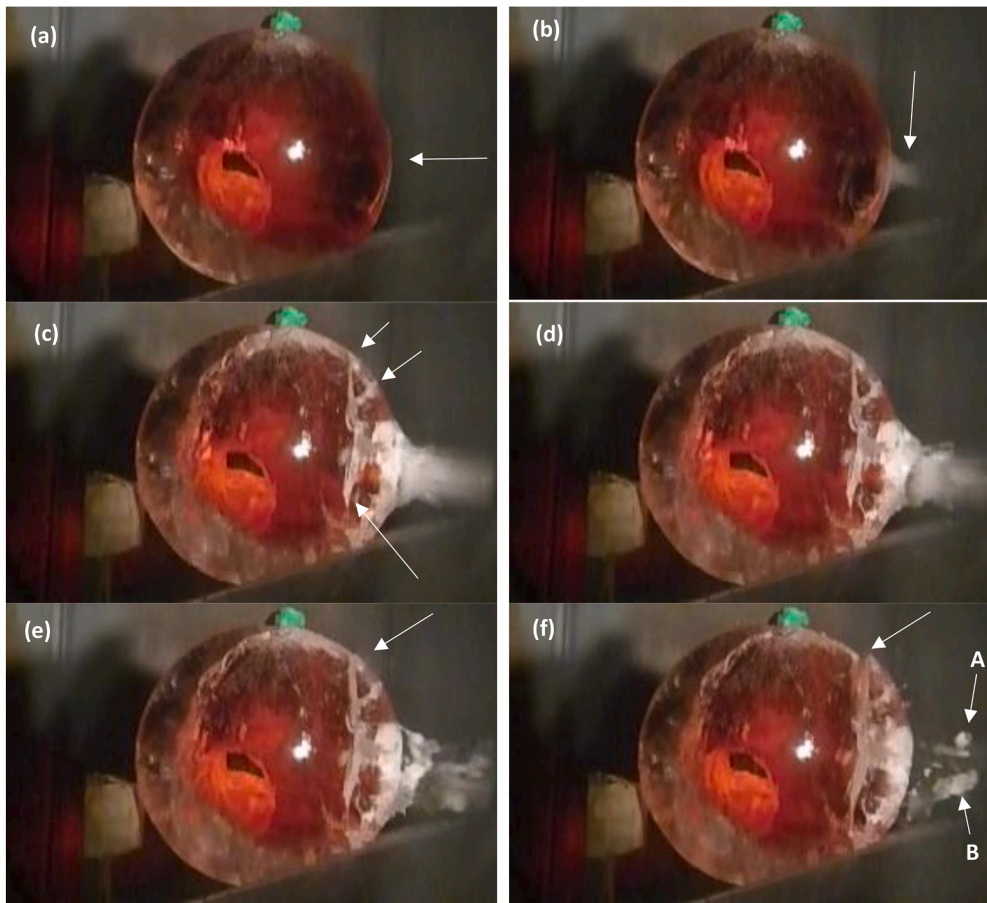
Fig. 4. Sequence of video stills showing the front of the ice shell (as seen from the impact direction which was from the right) detaching from the target in shot 9, after impact at 1.97 km s^{-1}. (a) Pre-impact. This target would not have been used in normal analysis, because the core can be seen in the lower right quadrant of the ice sphere, apparently stuck to the inside of the ice shell. (b) This is the first image showing an impact, the previous frame (undamaged target) was 0.017 s earlier. This frame is taken as t = 0. The classic fast ejecta plume (shown arrowed) can be seen moving rightward away from the impact point, but no fractures or cracks are yet visible in the bulk of the ice shell. (c) t = +0.017s . Extensive fracturing can now be seen (indicated with arrows), especially around the leading face of the sphere. (d) t = +0.051s. Larger ejecta is now beginning to lift off the surface of the ice sphere. (e) t = +0.1 s. The detached disk is now beginning to lift off the surface, and fall away. A gap is appearing between it and the rest of the ice sphere (e.g. see arrow). (f) t = +0.15 s. The front face has detached and is now moving away (the gap visible in (e) and marked with an arrow is growing larger, whilst the large ejecta (e.g. A and B) are now moving out of the field of view).

Table 3

Q^* as measured for ice spheres (dia. 18 – 20 cm), whose internal structures are as shown in Fig. 1.

Target Structure	Q^* (J kg^{-1})	Reference
Solid ice	18 ± 0.7	[13]
Ice surface with water filled interior	16.25 ± 1.35	[16]
Hollow ice sphere	25.5 ± 0.5	[15]
Ice surface, water layer beneath ice, and a central solid core	3.1 ± 0.1	This work

the largest to next largest and so on. This is similar to the result of disruption of hollow ice spheres just at the point of catastrophic disruption ($m_f/m_i = 0.53$ in Fig. 5b; data taken from [15]). As m_f/m_i falls to < 0.2 for hollow spheres, the shape of the distribution becomes near vertical and more convex shape (Fig, 5b), indicating that the largest fragments become near equal sized and then fragment mass falls off rapidly as the number of fragments increases. Fig 5c shows this effect also holds for water filled ice spheres (data taken from [16]).

In previous work on catastrophic disruption of asteroids, via both observations of asteroid families and computer simulation (e.g. [26–28]), the shape of the cumulative mass distribution of the fragments, has been held to indicate the degree of disruption. A concave appearance in the distribution indicating a sub-catastrophic impact and a convex appearance indicating a catastrophic disruption. Here the data in Fig. 5 suggest a similar trend is seen for both water-filled spheres (with and without cores) and hollow ice shells.

4. Discussion

The data presented here can be compared to that for catastrophic disruption of other types of ice spheres of similar size and varying internal structure (see Fig. 6). These target types include a solid ice sphere [13], the somewhat artificial scenario of a hollow ice sphere [15], and an ice surface with an interior filled with water [16]. The new data can be seen to be quite distinct in Fig. 6, and there are clear differences in Q^* depending on target type. Solid ice targets and those with an ice surface and liquid water interior, have similar Q^* values (around 16 – 18 J kg^{-1}). It was noted previously [15] that for hollow ice spheres, Q^* appears larger at (25.5 ± 0.5) J kg^{-1}, but the decrease in total mass that occurs due to the hollow interior almost exactly compensates for the increase in Q^*. This had been taken to indicate that the disruption was a surface layer phenomenon in these bodies. However, the results here for targets with a central core invalidate this hypothesis. There is an increase in the target mass here compared to equal size pure ice or water/ice targets. However, the difference (which arises from the relative densities of acrylic, 1180 kg m^{-3}, and ice/water) is small and does not explain the large decrease in Q^* by a factor of 5 – 6. The thickness of the ice shell here is comparable with that in past work, so this is also not a contributing factor. It thus appears the presence of a core has altered the development of the shock process, in effect weakening the target.

Early laboratory experiments on homogeneous basaltic targets [29] suggested that in rocky bodies, the on-set of catastrophic disruption was accompanied by core fragmentation, wherein the central core of the body was exposed as a fragment. Later experimental work, by amongst others [30–33], confirm this in high speed impacts on various rocky targets. However, [34] observed that catastrophic disruption of icy targets behaved differently. This was confirmed by [14] who reported that solid ice targets break apart due to cone-like penetration by the
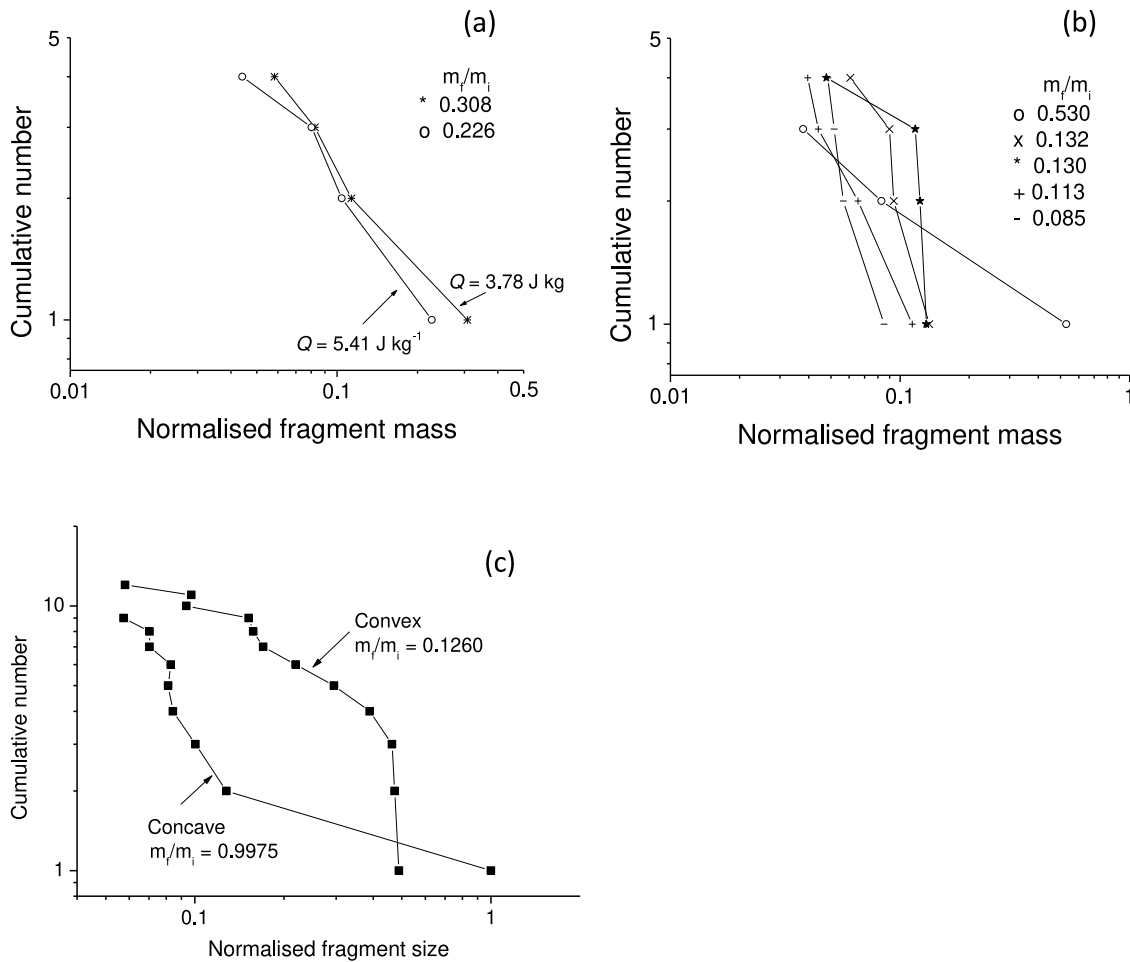
Fig. 5. Cumulative frequency vs. fragment mass (normalised to total mass). The degree of disruption for each data set is indicated by the normalised mass of the largest fragment in each event. (a) This data. The two events (shots 7 and 8, Q = 3.78 and 5.41 J kg^{-1} respectively)) are in the catastrophic disruption regime, with $Q > Q^*$ (here 3.1 J kg^{-1}). (b) Data from hollow ice spheres (taken from [15], table 2). In general, in (a) and (b), at $m_f/m_i \approx 0.2 - 0.5$, the distribution is a diagonal straight line. As the degree of disruption increases, an increasingly convex, initially near vertical distribution of near equal sized largest fragments emerges. (c) Catastrophic disruption of water filled ice spheres, reproduced from Fig. 5 in [16]. The concave shape in (c) at $m_f/m_i >> 0.5$ indicates a cratering rather than disruption event, whilst the convex shape at $m_f/m_i << 0.5$ is typical of a catastrophic disruption.

impactor, which results in vertical and horizontal fractures originating from the base and sides of the crater that form in the ice.

However, when discussing the disruption of layered targets there is a new issue, namely the influence of the internal structure on the disruption process. Previously, it has been shown for a body with an icy mantle directly over an ice:silicate core (i.e. a two layer body), that a thin surface ice layer, taken as t/d in the range of 1 – 2, made no difference to the disruption process or Q^* [35]. In [35] t/d was varied by changing the mantle thickness, so that t/d ranged from 1 to 7. As mantle thickness increased to >6 times projectile diameter, a complicated pattern of behaviour emerged: At $Q < Q^*$, there was more mass removed than expected from simple cratering, suggesting that mass is more easily lost from the surface layer when there is a core of different material beneath it. When the mantle was relatively thick compared to the projectile size, Q^* increased by a factor of 1.8 compared to that for a target of just the core material (ice:silicate in that case), or one with a large core and thin ice surface layer.

Laboratory disruption of core:mantle targets for rocky bodies has also been reported [36]. Along with the ratio t/d (0.233 – 7.53), the ratio of core mass to total target mass (R_{CM}) was flagged as a key parameter in [36]. As well as the extreme cases of $R_{CM} = 1$ (only a core present), and 0 (a target body made up of only mantle material), in [36] R_{CM} was varied over the range 0.0026 – 0.860. It was found in [36] that they

could describe their work by 4 types of outcomes, which, listed in increasing order of severity are: IV: Core totally/partially covered by mantle with crater in the mantle, III: Core intact and mantle fragmented and removed, II: Core exposed with damage to its surface, and I: Core disrupted. Only the equivalent of outcomes III and IV are observed here, with type IV equivalent to a cratering event here, and type III being a catastrophic disruption event.

Here however, there is the added complication of a third layer in the target (the core beneath an internal ocean), and this has influenced the outcome of the impact, significantly lowering Q^*. A sequence of increasing damage as Q is increased can be described as summarised in Table 4. It is possible that the results of future work will require category IV (not observed here), i.e. a category which includes damage to the core being observed before full disruption occurs. The presence of category IV-like features in an impact may well depend on the relative thickness of the surface ice and water ocean, and the radius of the central core. Indeed, technically, if the central core were large enough it would have over 50% of the total target mass, so simply removing all of the outer two layers would not result in a catastrophic disruption event unless the core itself was damaged and either broken apart or had material removed from it via cratering.

To gain further insights into the disruption process, modelling is required. The key feature of the tri-layered targets, seems to lie in the
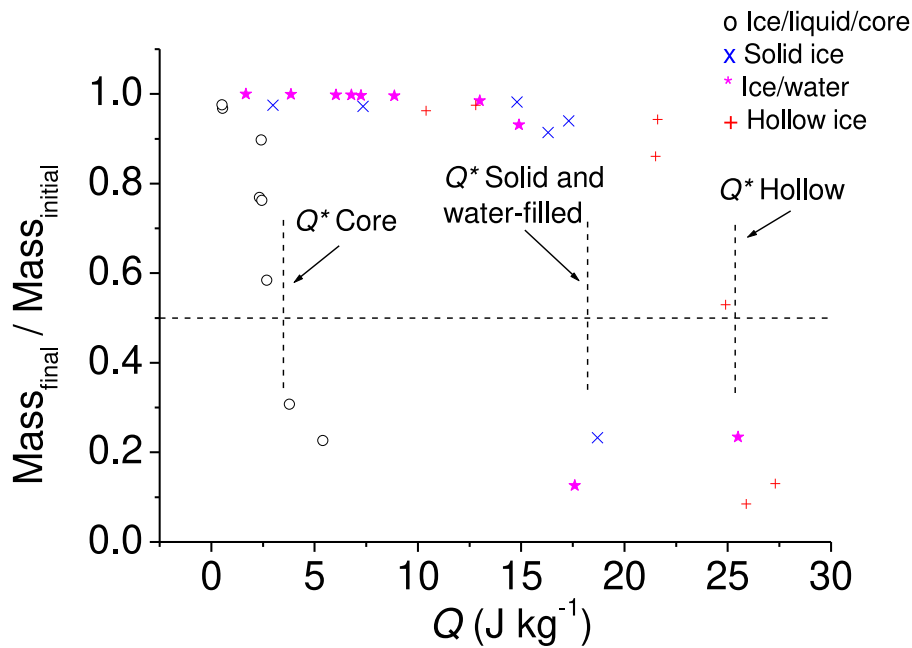
Fig. 6. Compilation of data for target mass ratio (final/initial) vs. impact energy density Q. The horizontal dashed line is at mass ratio = 0.5, which defines Q^*. Three sets of behaviour can be seen. The targets with an ice surface, water layer and solid core, have $Q^* \approx 3$ J kg^{-1}. The solid ice [13] and the water filled ice targets [16] have $Q^* \approx 16 - 18$ J kg^{-1}. The hollow ice spheres [15] have $Q^* \approx 25$ J kg^{-1}.

Table 4

Impact outcomes for layered targets with an icy surface layer as the impact energy density Q increases. Category IV is not observed here but is reasonably postulated.

Outcome category	Characteristics
I	Relatively small crater in surface ice layer
IIa	Larger crater in surface ice layer with (non-penetrating) radial cracks propagating to several times crater diameter
IIb	Even larger crater, with onset of concentric cracks and some cracks penetrate the ice layer
III	Penetration of main crater in the surface ice into the second layer
IV	Removal of surface layer and part of the interior ocean, plus damage to the core (not observed here)
V	Disruption of the whole body.

presence of surface and core materials with strength, decoupled by an intermediate water layer with no shear strength. In [37], hydrocode modelling of the response of Enceladus to impact was performed. Two main cases were considered, a two layered target body with an icy mantle directly over a rocky core, and a three layered structure where core and mantle were separated by a water layer. Although [37] did not focus on catastrophic disruption, what they reported was that energetic impacts which penetrated the ice shell, can interact with the core. Further, the presence of the internal structure, concentrates the resulting deformation processes into the icy surface layer.

Taken with our experimental results here, we suggest that the presence of the core beneath the water layer, reflects shock waves towards the surface ice. This surface layer has already been weakened, and then undergoes further damage. This in turn causes the observed catastrophic disruption failure at a lower energy density than in the absence of the core.

5. Conclusions

The work described herein represents a first attempt to tackle the issue of a tri-layered icy ocean world at laboratory scales. What is revealed in the work is that the presence of a three layer structure with a central core, significantly influences the outcome of the impact event, with catastrophic disruption occurring at a notably lower energy density than for solid ice or two layered ice/water targets.

The relative thicknesses of the layers in the targets here each layer (core approximately 25%, water layer 55% and surface ice layer 20% of the total target radius) are not in good agreement with any particular icy ocean world, with the core being too small, and the ocean layer too thick. This is due to technical difficulties with making targets with these structures. Future work should therefore focus on having layering more representative of the icy ocean worlds and seeing how, in particular, the presence of a larger core and shallower ocean than here, influences the value of Q^*. The relative roles of the ice and liquid water in the surface two layers can then also be investigated for thick and thin ice surface layers. Further, when there is a shallow ocean, how the core is damaged in the impact process should also be studied. In future work a variety of core materials could also be used, including rocky and metal cores. Indeed if a porous core were used it would be possible to have a water saturated core. Seeing how Q^* varies with such changes would help provide insights into how the core is influencing the disruption process.

CRediT authorship contribution statement

M.J. Burchell: Conceptualization, Methodology, Formal analysis, Writing – original draft, Writing – review & editing, Funding acquisition. **K.H. Harriss:** Methodology, Investigation, Formal analysis, Writing – review & editing.

Declaration of Competing Interest

The authors declare that they have no known competing financial interests or personal relationships that could have appeared to influence the work reported in this paper.

Acknowledgments

References

[1] Carr MH, Belton MJ, Chapman CR, Davies ME, Geissler P, Greenberg R, Veverka J. Evidence for a subsurface ocean on Europa. Nature 1998;391(6665):363–5.

[2] Pappalardo RT, Belton MJS, Breneman HH, Carr MH, Chapman CR, Collins GC, Williams KK. Does Europa have a subsurface ocean? Evaluation of the geological evidence. Journal of Geophysical Research: Planets 1999;104(E10):24015–55.

[3] Sparks WB, Hand KP, McGrath MA, Bergeron E, Cracraft M, Deustua SE. Probing for evidence of plumes on Europa with HST/STIS. Astrophys. J. 2016;829:121 (21 pages).

[4] Kivelson G, Khurana KK, Volwerk M. The permanent and inductive magnetic moments of Ganymede. Icarus 2002;157:507–22.

[5] Khurana KK, Kivelson MG, Stevenson DJ, Schubert G, Russell CT, Walker RJ, Polanskey C. Induced magnetic fields as evidence for subsurface oceans in Europa and Callisto. Nature 1998;395(6704):777–80.

[6] Waite JH, Combi MR, Ip WH, Cravens TE, McNutt RL, Kasprzak W, Yelle R, Luhmann J, Niemann H, Gell D, Magee B, Fletcher G, Lunine J, Tseng WL. Cassini ion and neutral mass spectrometer: Enceladus plume composition and structure. Science 2006;311(5766):1419–22.

[7] Nimmo F, Spencer JR, Pappalardo RT, Mullen ME. Shear heating as the origin of the plumes and heat flux on Enceladus. Nature 2007;447(7142):289–91.

[8] Čadek O, Tobie G, Van Hoolst T, Masse M, Choblet G, Lefevre A, Mitri G, Baland RM, Behounkova M, Bourgeois O, Trinh A. Enceladus's internal ocean and ice shell constrained from Cassini gravity, shape, and libration data. Geophys. Res. Lett. 2016;43(11):5653–60.

[9] Lorenz RD, Stiles B, Kirk RL, Allison MD, Persi del Marmo P, Iess L, Lunine JI, Ostro SJ, Hensley S. Titan's rotation reveals an internal ocean and changing zonal winds. Science 2008;319:1649–51.

[10] Béghin C, Randriamboarison O, Hamelin M, Karkoschka E, Sotin C, Whitten RC, Berthelier JJ, Grard R, Simões F. Analytic theory of Titan's Schumann resonance: constraints on ionospheric conductivity and buried water ocean. Icarus 2012;218(2):1028–42.

[11] Hemingway D, Nimmo F, Zebker H, Iess L. A rigid and weathered ice shell on Titan. Nature 2013;500(7464):550–2.

[12] Harriss KM, Burchell MJ. Hypervelocity impacts into ice crust targets: investigating the effects of ice crust thickness and subsurface density on crater morphology. Meteoritics and Planetary Science 2017;52:1505–22.

[13] Leliwa-Kopystynski J, Burchell MJ, Lowen D. Impact Cratering and Break-up of the Small Bodies of the Solar System. Icarus 2008;195:817–26.

[14] Arakawa M. Collisional Disruption of Ice by High-Velocity Impact. Icarus 1999;142:34–45.

[15] Harriss KH, Burchell MJ. Catastrophic Disruption of Hollow Ice Spheres. The Planetary Science Journal 2020;1:19.

[16] Burchell MJ, Landers K, Harriss KH, Price MC. Catastrophic Disruption of Icy Bodies with Sub-Surface Oceans. Icarus 2020;336:113457.

[17] Burchell MJ, Cole MJ, McDonnell JAM, Zarnecki JC. Hypervelocity Impact Studies Using the 2 MV Van de Graaff Dust Accelerator and Two Stage Light Gas Gun of the University of Kent at Canterbury. Meas. Sci. Tech. 1999;10:41–50.

[18] Hibbert RH, Cole MJ, Price MC, Burchell MJ. The hypervelocity impact facility at the University of Kent: Recent upgrades and specialised facilities. Procedia Engineering 2017;204:208–14.

[19] Arakawa M, Maeno N, Higa M. Direct observation of growing cracks in ice. J. Geophysical Research 1995;100:7539–47.

[20] Arakawa M, Shirai K, Kato M. Shock wave and fracture propagation in water ice by high velocity impact. Geophysical Research Letters 2000;27(3):305–8.

[21] Grey IDS, Burchell MJ, Shrine NRG. Scaling of Hypervelocity Impact Craters in Ice with Impact Angle. J. of Geophysical Research E. 2002;107(E10):5076. https://doi.org/10.1029/2001JE001525.

[22] Asphaug E. Similar-sized collisions and the diversity of planets. Chemie der Erde-Geochem 2010;70(3):199–219. https://doi.org/10.1016/j.chemer.2010.01.004.

[23] Leinhardt ZM, Stewart ST. Collisions between gravity-dominated bodies. I. Outcome regimes and scaling laws. Astrophys. J. 2012;745(1):79. https://doi.org/10.1088/0004-637X/745/1/79.

[24] Yasui M, Arakawa M, Yoshida Y, Matsue K, Takano S. Effects of oblique impacts on the impact strength of porous gypsum and glass spheres: Implications for the collisional disruption of planetesimals in thermal evolution. Icarus 2020;335:113414.

[25] Movshovitz N, Nimmo F, Korycansky DG, Asphaug E, Owen JM. Impact disruption of gravity-dominated bodies: New simulation data and scaling. Icarus 2016;275:85–96.

[26] Tanga P, Cellino A, Michel P, Zappalà V, Paolicchi P, Dell'Oro A. On the size distribution of asteroid families: The role of geometry. Icarus 1999;141:65–78.

[27] Durda DD, Bottke Jr, W F, Nesvorný D, Enke BL, Merline WJ, Asphaug E, Richardson D. Size–frequency distributions of fragments from SPH/N-body simulations of asteroid impacts: Comparison with observed asteroid families. Icarus 2007;186:498–516.

[28] Leliwa-Kopystynski J, Burchell MJ, Włodarczyk I. The impact origin of Eunomia and Themis families. Meteoritics & Planetary Science 2009;44(12):1929–35.

[29] Fujiwara A, Kamimoto G, Tsukamoto A. Destruction of basaltic bodies by high-velocity impact. Icarus 1977;31:277–88.

[30] Morris AJW, Price MC, Burchell MJ. Is the large crater on asteroid (2867) Steins really an impact crater? Astrophysical Journal Letters 2013;774:L11. https://doi.org/10.1088/2041-8205/774/1/L11 (5pp).

[31] Durda DD, Bagatin AC, Alemañ RA, Flynn GJ, Strait MM, Clayton AN, Patmore EB. The shapes of fragments from catastrophic disruption events: Effects of targets shape and impact speed. Planetary and Space Science 2015;107:77–83.

[32] Michikami T, Hagermann A, Kadokawa T, Yoshida A, Shimada A, Hasegawa S, Tsuchiyama A. Fragment shapes in impact experiments ranging from cratering to catastrophic disruption. Icarus 2016;264:316–30.

[33] Morris AJW, Burchell MJ. Laboratory tests of catastrophic disruption of rotating bodies. Icarus 2017;297:91–8.

[34] Fujiwara, A., Cerroni, P., Davis, D., Ryan, E., Di Martino, M., Holsapple, K., and Housen, K., 1989. Experiments and Scaling Laws for Catastrophic Disruption. In: Binzel R.P., Gehrels M.S., Matthews M.S., (Eds.), Asteroids II. Univ. of Arizona Press, Tucson, pp. 240–265.

[35] Lightwing, A., and Burchell, M.J., 2008. Catastrophic Disruption of Icy Core-Mantle Bodies in the Laboratory. Lunar and Planetary Science Conference XXXIX, abstract #1842.

[36] Okamoto C, Arakawa M. Experimental study on the impact fragmentation of core–mantle bodies: Implications for collisional disruption of rocky planetesimals with sintered core covered with porous mantle. Icarus 2008;197:627–37.

[37] Monteux J, Collins GS, Tobie G, Choblet G. Consequences of large impacts on Enceladus' core shape. Icarus 2016;264:300–10.